PAPER

Check for updates

Semitransparent color tunable perovskite solar cells with 3D pillar structure

Vikas Sharma, [ID] Ouriel Bliah, Tal Binyamin, Shlomo Magdassi* and Lioz Etgar [ID] *

Semi-transparent, flexible, and coloured solar cells are highly attractive for building-integrated photovoltaics (BIPV) and indoor PV applications. Here, we report the fabrication of low-temperature processed, flexible, semi-transparent, and colour-tunable perovskite solar cells. Optical transparency is achieved through 3D-printed micro-patterned pillars, using an eco-friendly, solvent-free monomer. Colour tunability is controlled by the thickness of the top transparent electrode, designed as a dielectric−metal−dielectric stack. These semi-transparent devices selectively reflect light at specific wavelengths (perceived as colour), enabling retrofitting for existing windows. The fabrication process integrates plasma-assisted low-temperature deposition of a charge transport layer, inkjet printing of 3D pillars, and coloured transparent contact without altering the perovskite composition. The flexible semi-transparent devices demonstrated a power conversion efficiency of 9.2%, an average visible transparency of 35%, and excellent bending stability. This method offers a general strategy for realizing semi-transparent perovskite solar cells with diverse compositions, without requiring bandgap modification.

Broader context

The transition to renewable energy requires not only efficient but also versatile photovoltaic technologies that can integrate into the built environment and indoor applications. Conventional opaque solar modules are unsuitable for windows or flexible substrates, limiting their deployment in urban landscapes and portable devices. Perovskite solar cells have rapidly emerged as promising candidates due to their high efficiencies and low-cost processing, yet challenges remain in achieving transparency, colour control, and flexibility without compromising performance or relying on toxic processing routes. This work addresses these challenges by introducing a scalable, eco-friendly approach to fabricate semitransparent, colour tunable, and mechanically flexible perovskite solar cells. By employing 3D-printed optical pillars and low-temperature processing, transparency and aesthetics are engineered without modifying the perovskite absorber itself. This strategy enables coloured and flexible devices that can be retrofitted onto existing windows and curved surfaces, while maintaining competitive power conversion efficiencies and operational stability. Beyond advancing the design of building-integrated photovoltaics (BIPV), these results point to broader opportunities for sustainable manufacturing of functional, aesthetically adaptable solar technologies.

Introduction

The next era of solar cells will surpass conventional solar farms and terrestrial panels.[1] New applications, such as building-integrated photovoltaics (BIPV), are needed to address clean energy concerns.[2] To achieve the BIPV goals, a semi-transparent solar cell that can adjust light transmission while generating electricity concurrently must be developed.[3] Perovskite solar cells (PSCs), the leading next-generation thin-film PV technology, have achieved remarkable efficiencies (26% for single-junction, 34% for Si-perovskite tandem).[4,5] Along with efficiency, PSC provides adequate transparency, defect tolerance, low weight, easy processability, and low-cost technology, making it suitable for BIPV applications. Beyond BIPV, light-weight and flexible solar cells can be utilised in various applications, including tandem structures, self-energy convertible tents, bags, vehicle-integrated PV, indoor PV, agricultural PV, and intelligent electronic gadgets.[6] Despite these advantages, fabricating flexible, semi-transparent perovskite solar cells remains challenging due to limitations of high process temperature, especially for metal oxide-based charge transport layers. Additionally, sputter damage can occur during the deposition of transparent electrodes.[7,8] As a result, various annealing techniques have been established to enable metal oxide layer formation at lower temperatures; however, the performance of devices based on such layers does not reach that of high-temperature processed solar cells.[8,9] The poor performance is due to the absence of proper crystallinity, surface morphology, and electronic properties. To improve the performance, it is possible to add an additive, such as vacuum annealing, doping, and interface modification through extra layer coating, which makes the fabrication process more complex and less suitable for industrial production.

The Hebrew University of Jerusalem, Institute of Chemistry, The Center for Nanoscience and Nanotechnology, Casali Center for Applied Chemistry, Jerusalem 9190401, Israel. E-mail: magdassi@mail.huji.ac.il; lioz.etgar@mail.huji.ac.il

The primary goal of semi-transparent solar cells is to provide adjustable average visible transmittance (AVT) with high power conversion efficiency (PCE).[10] The semi-transparent mode prevents metal-induced degradation in PSC that may occur through metal migration or iodine–metal corrosion, leading to improved stability.[11] The way to achieve semi-transparent PV is mainly in two directions: (i) wavelength-selective transparent PV, where the solar cell absorbs selective energy, which makes it semitransparent, and (ii) non-wavelength-dependent semi-transparent PV, where the active material absorbs light in a wide spectrum, including the visible range. In this technology, there is a direct trade-off between efficiency and AVT, and it is mostly used in BIPV.[12] With distinct features and benefits, extensive research is ongoing in the composition engineering of photoactive materials, bandgap tuning, thickness modification, and the integration of additional layers, which has led to various semi-transparent thin-film solar cell technologies. Currently, research is focused on semi-transparent PV based on new semiconductors, such as halide perovskites. The lab-scale devices based on these technologies generally exhibit a PCE of ~10% with an AVT of ~20%.[13,14] The transparency of such cells is controlled by altering the bandgap of materials or the thickness of the absorber layer. However, issues associated with modified composition and band gap tuning, such as instability, halide separation, deep-level defect formation,[15,16] and poor performance in terms of AVT and PCE. Therefore, semi-transparent PV requires an unconventional approach to improve the fabrication process and achieve the desired results with commercial viability.[12,17] There is a research gap and scope, especially in controlling the transparency without changing the bandgap. Researchers focused on the island growth of perovskite, honeycomb geometry, grid structure, and nano-pillar-based devices to achieve transparency without altering the bandgap.[17–19] Our previous report shows that solvent-based monomer ink is suitable for pillar printing of semitransparent electrodes; however, in that case, the main limitation was the non-green process.[20,21] To make it industrially viable, it is required to make the inks with non-hazardous, eco-friendly materials. Semi-transparent perovskite solar cells (ST-PSCs) have progressed rapidly in the last few years as researchers optimize the trade-off between transparency and power generation by maximizing light utilization efficiency (LUE), the product of power conversion efficiency (PCE) and average visible transmittance (AVT). Advances in interfacial engineering and molecular dipole tuning have demonstrate raised LUE in lab devices, enabling practical LUE values and improved operational stability for smart-window applications.[10,22] Fabrication paths include scalable solution printing (inkjet, slot-die, roll-to-roll) that allows for patterning and local AVT control, as well as vacuum/thermal evaporation or co-evaporation, which yields ultra-thin, uniform absorbers with improved color neutrality and higher device uniformity. Both routes now display record LUE demonstrations under ambient-compatible processes.[23–25] Strategies to tune color have matured beyond simple tinted absorbers: dielectric/metal/dielectric (DMD) electrodes, 1D photonic crystals, and microcavity/structural-colour architectures produce vivid, angle-tolerant colors while preserving photon harvesting *via* spectrally selective reflection or transmission. These photonic approaches enable colored ST-PSCs for BIPV without large LUE penalties when co-optimized. Remaining challenges include standardized LUE metrics, long-term outdoor stability, and flexibility management for commercial deployment.[26,27] Currently, austheic coloured solar cells are one of the prime requirements for BIPV applications.[28,29] To achieve a coloured cell, it is necessary to add an extra layer of coloured material over the cell or to incorporate reflective pigments, which reduces efficiency and increases the number of processes and fabrication costs.[30–33] Another route is to use a sputter deposition of an Indium-based transparent electrode with different thicknesses, which makes the solar cell expensive due to the scarcity of Indium, sputter damage, and high-temperature processing.[30,34] An Additional option is laser-based hole creation or ablation, which causes material waste and exposure of different layers to the ambient environment.[12] At the same time, dielectric–metal–dielectric (DMD) based transparent contact deposition at room temperature has shown stability in ambient conditions and emerges as the best option for semi-transparent PV.[35,36]

Here, we present altering the transparency and colour of halide perovskite solar cells using 3D-printed structures. We developed a low-temperature electron transport layer [ETL] process for the flexibility devices. The control over the device's transparency was achieved by printing 3D transparent pillars, which function as "optical holes" at micrometric dimensions. Moreover, the fabrication of the pillars is performed using inkjet printing of a solvent-free, UV-curable monomer-based ink, which is non-hazardous and suitable for future large-scale fabrication. Our approach introduces a transparent top electrode (MoO_x–Au–MoO_x) that transmits light to the perovskite layer while selectively reflecting specific wavelengths, producing coloured semitransparent solar cells. The reflected light of the cell is controlled by the thickness of the top transparent electrode. These coloured, transparent, and flexible cells can be used for existing windows *via* a retrofitting process.

Results and discussion

Fig. 1 schematically presents the flexible solar cell structure and the related process. The first layer (ETL) was fabricated by the deposition of tin oxide (SnO_2) in open air, followed by thermal annealing (100 °C) and immediate plasma treatment to obtain a uniform layer on a flexible ITO coated PEN substrate. Following this stage, polymeric 3D pillars that enable transparency were fabricated by inkjet printing. The next stage is the deposition of mixed halides perovskite solution ($Cs_{1−x}FA_xPb(Br_{1−x}I_x)_3$) ($x = 0.85$, FA = formamidinum) by spin coating, and subsequent spin coating of the hole transport layer (HTL), Spiro-OMeTAD. The final step is the deposition of the top transparent contact (MoO_x–Au–MoO_x) using a thermal evaporator. The thickness of the top MoO_x layer was modified to obtain various colours for the solar cells (as explained below). Light falling on the back electrode generates different colours due to reflection, leading to colored solar cell fabrication.
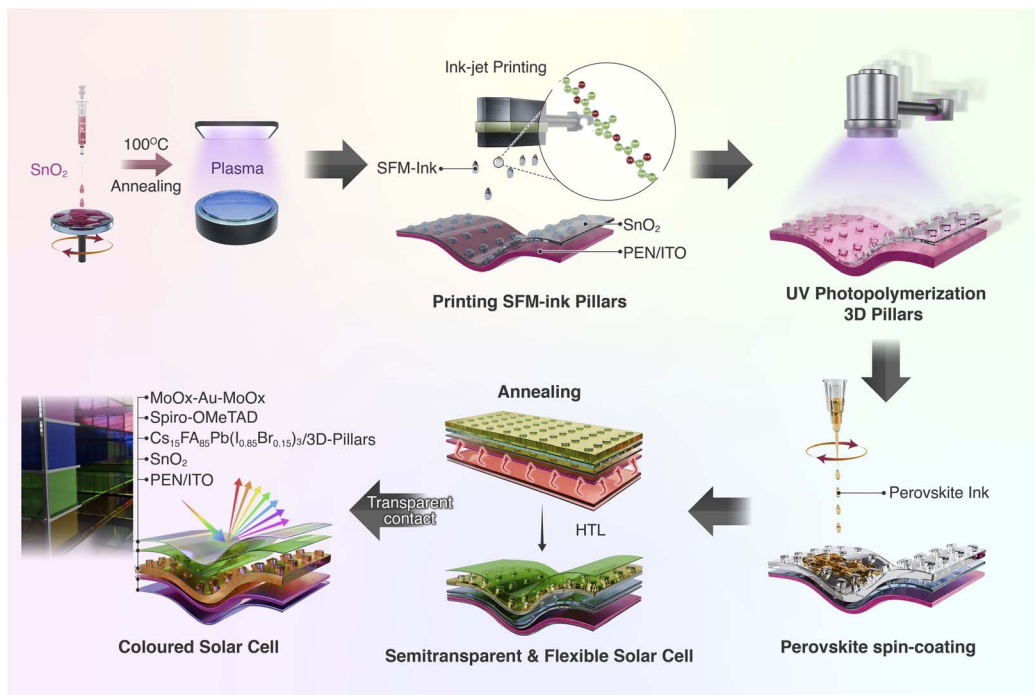
Fig. 1 Schematic presentation of the main steps involved in the fabrication of a colourful, semi-transparent, flexible perovskite solar cell.

Plasma-assisted low-temperature ETL

In the first step of fabrication, tin oxide (SnO_2) has been chosen as the ETL layer due to its advantages, including suitable energy level alignment and good electron conductivity.[37,38] However, the ETL layer based on SnO_2 typically requires a high annealing temperature, which is not suitable for flexible substrates. Therefore, it was required to develop a low-temperature fabrication process. Commercial colloidal SnO_2 was deposited by spin coating, followed by thermal annealing. Three temperatures were evaluated: 60 °C, 100 °C, and 180 °C. The samples annealed at 60 °C, 100 °C, and 180 °C are denoted as low-temperature annealed (LTA), medium-temperature annealed (MTA), and high-temperature annealed (HTA), respectively. The ETL layer was annealed for 10 minutes at that temperature, followed by 10 minutes of oxygen plasma treatment. As a reference, a SnO_2 layer was deposited and annealed at common conditions (180 °C for 30 minutes).[39,40] A series of electrical, optical, and structural measurements was performed to determine the best ETL.

Fig. 2a shows the *I–V* curves of the LTA, MTA, and HTA layers, from which it can be concluded that the conductivity of the SnO_2 increases with the increase of the annealing temperature. The contribution of ITO resistance is considered equally in all layers. Measured resistance plots for different SnO_2 layers are shown in Fig. S1, which assist in the charge (electron) extraction and transport at the perovskite/ETL interface in the solar cell. It should be noted that the three SnO_2 films exhibit similar surface roughness, ranging from 2 to 5 nm (Fig. 2b–d), in agreement with the SEM imaging (Fig. S2), indicating compatibility with solar cell fabrication. High and nearly similar optical transparency of the different ETL layers included in Fig. S3. The

Raman and FTIR spectra shown in Fig. S4 indicate that the SnO_2 layers at different annealing conditions have nearly the same in-plane oxygen vacancy concentration, which assists in the conductivity of the layer.[7,41] The chemical state of the SnO_2 films determined by XPS measurements[7,42,43] is shown in Fig. 2e–h. Fig. 2e–g shows peaks for oxygen (O 1s) peak deconvoluted into 3 peaks: Sn–O, O–H, and O–C. The fraction of Sn–O remains nearly the same in all layers, but the fraction of the O–C bond increases with the annealing temperature. The O–H bond is maximal at the LTA, 5.4%, decreasing to 3.6% in the MTA and 1.8% in the HTA layer. The varying number of O–H bonds can be attributed to water traces that remain in the sample and decrease as the annealing temperature increases.

The perovskite composition used in this work is the double-cation, double-halide lead-based perovskite, which is considered more stable than the triple-cation perovskite with methylammonium.[44–46] Here, the two cations are FA (formamidium) and Cs (caesium), with iodine and bromine as the halides, having the chemical formula $FA_{0.85}Cs_{0.15}Pb(I_{0.85}Br_{0.15})_3$. The perovskite was then spin-coated on the various SnO_2 layers, and the surface was evaluated by a scanning electron microscope, as shown in Fig. 2i–k. The SEM images show dense and pin-hole-free layers for all samples. The most prominent change detected between the different SnO_2 layers is in XPS measurements. In XPS, we found that the O–H bond amount is changed for different SnO_2 layers, leading to small variation in the perovskite film. The transmittance and absorbance spectra of the halide perovskite layer are similar to all SnO_2 layers (Fig. S5). The photoluminescence (PL) and time-resolved photoluminescence (TRPL) data of the perovskite layer coated on different SnO_2 layers are shown in Fig. S6a and
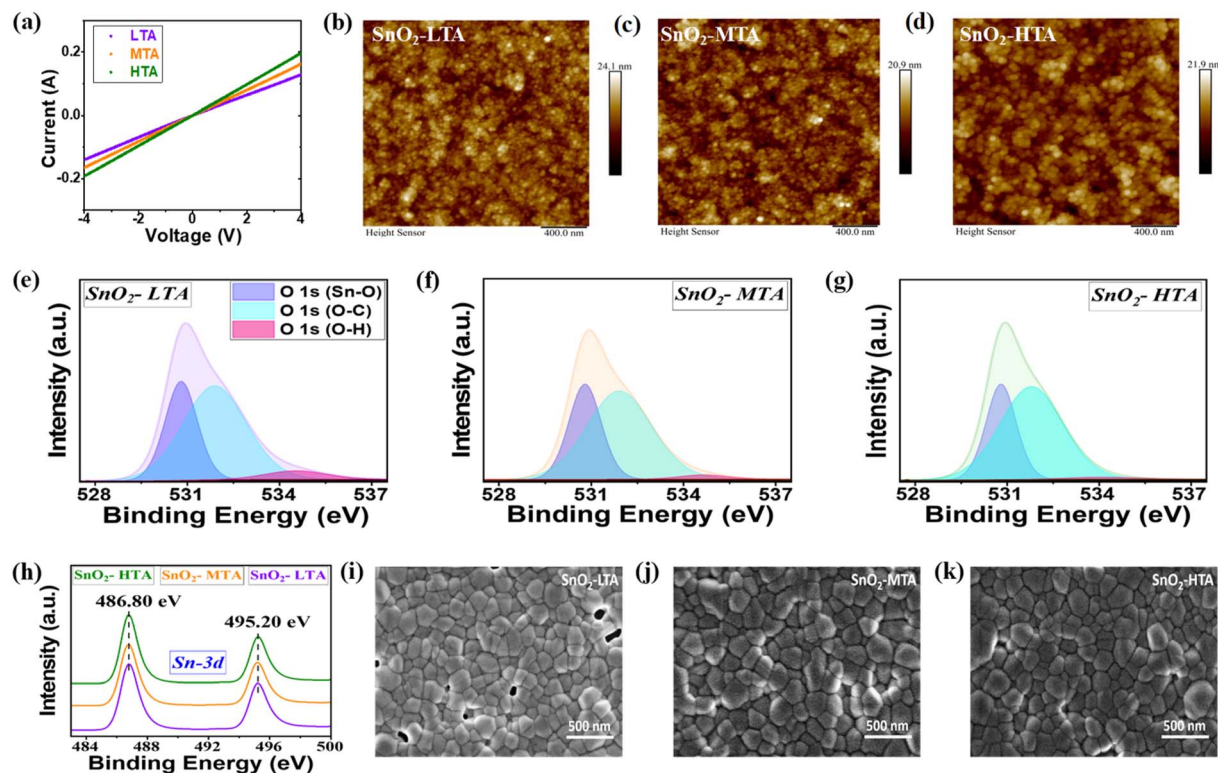
Fig. 2 (a) *I−V* measurement for the LTA, MTA, and HTA SnO$_2$ films. (b–d) Surface morphology for the SnO$_2$ films using AFM. (e–g) XPS analysis of oxygen (O 1s). (h) Sn 3d XPS spectra. (i–k) Top-view SEM images of the mixed cation mixed halide perovskite, deposited on the different SnO$_2$ layers.

b, respectively. The PL intensity indicates better charge injection for the LTA and MTA compared to the HTA samples. The lifetime (based on bi-exponential fitting) for the LTA samples is shorter than that for the MTA and HTA (Table ST1), further supporting the efficient injection of charges from the perovskite to the ETL. Finally, complete solar cells were fabricated using the above SnO$_2$ layers. The *I–V* curves and PV parameters are presented in Fig. S7a and b, showing a slightly higher average PCE for the HTA and MTA (Fig. S7c) compared to the LTA sample. The FF and V_{oc} of the MTA-fabricated cells are higher than the other two cells (Fig. S7d–f). Based on the above results, subsequent experiments were conducted with MTA layers.

Transparency modulation by 3D printed structures

The focus of this stage is on controlling the transparency of the cells. To achieve this, arrays of 3D polymeric pillars were fabricated using ink-jet printing of a UV-curable, solvent-free ink, as described in the Experimental section. The chemical structure of the ink components is shown in Fig. S8. Since the wetting of the composition was too rapid and resulted in irregular shapes, the ink includes a levelling agent and a tri-functional monomer (Fig. S9a and b), resulting in regular, circular shapes. The ink was stable for a long time (6 months), with a viscosity of 16 Pa s (Fig. S10) and full transparency on several substrates as seen in Fig. S11. The tri-functional monomer enabled crosslinking, resulting in a polymer that is insoluble in the solvent used in the next step of solar cell

fabrication, the perovskite solution. As shown in Fig. S12, the 3D pillars are stable in the solvents used for the subsequent steps, DMF, DMSO, CB, and IPA. The top and cross-sectional views of the printed pillars are shown in the SEM images (Fig. 3a and b).

The control of the solar cell's transparency can be achieved by controlling the fraction of the solar cell's surface that is covered by the pillars. The pillar's surface coverage was controlled by changing the distance between the pillars, 2000, 1500, and 1000 microns. The pillars are shown in Fig. 3c. Following pillar fabrication, the perovskite layer was spin-coated onto the array. The optical and SEM images after the perovskite coating over the pillars indicate that there is no morphological or grain boundary difference in the perovskite layer between the pillars (Fig. S13–S15). The wave-like pattern was observed near the pillars due to the combined effect of the pillar obstacle on the flow of the perovskite solution during coating. Moreover, the pillar structure support upscaling deposition techniques, such us: printing, evaporation and slot die coating of the perovskite layer on the whole surface, due to the difference in the wettability of the perovskite and the pillars. EDX measurements (Fig. 3d and e) revealed that the surroundings of the pillars are not covered by the perovskite. Optical studies confirmed that transparency increased with pillar distance, reaching 34% for 1000 pillars (Fig. 3f), while absorption intensity decreased due to reduced active area (Fig. 3g). While for 1500 pillars the AVT is 28% and with no
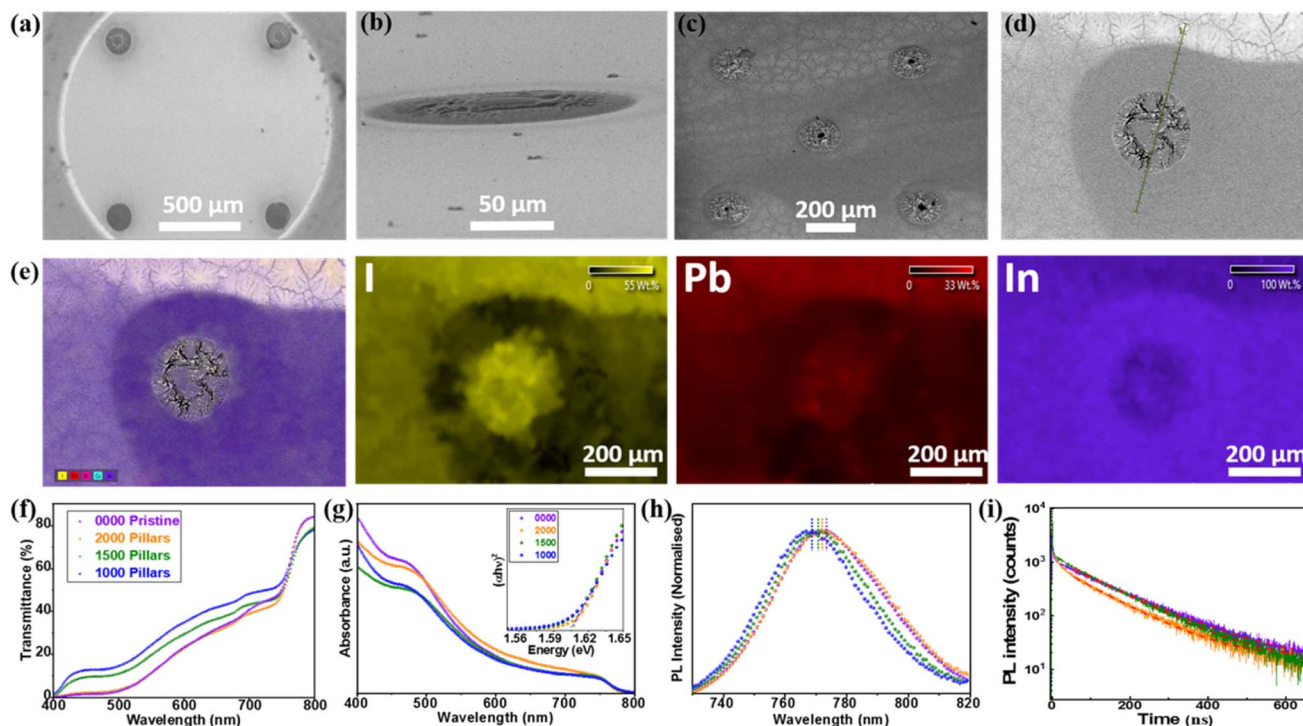
Fig. 3 (a) SEM Imaging of 3D polymer pillars printed on flexible PEN substrates using an inkjet printer. (b) Cross-sectional image of printed pillars. (c) Top view of 3D-printed pillars embedded in the perovskite layer. (d and e) EDX imaging of different components of the pillar, halide perovskite, and bottom layers. (f) Control of the transparency in the visible spectrum with the change in 3D printed polymer pillar concentration. (g) Absorption spectra for halide perovskite layer incorporating different 3D pillar concentrations, the inset shows the bandgap of the perovskite film with pillars. (h) Normalised PL for halide perovskite layer with different pillar concentrations. (i) TRPL measurement is used for lifetime calculation of the perovskite layer with various pillar structures.

pillars (same perovskite concentration) the AVT is 25%. Ritzer *et al.* used the laser drilling to get the translucent solar cells with PCEs of 9.0% at 32% AVT for single junction and 11.1% at 31% AVT for tandem structure.[12] While colored cells were reported by Wang at el with efficiency ranges from 11.2–13.3% for various colours where the transparency is *ca.* 20% in the visible range.[31] In this work the bandgap remained unchanged, and only minor variations in PL spectra (blue shift from 773 to 768 nm, Fig. 3h) and TRPL lifetime (133 ns to 107 ns, Fig. 3i) were observed, indicating slightly higher recombination but no significant impact on charge carrier dynamics due to pillar inclusion.

Fabrication of semi-transparent solar cells

The fabrication of semi-transparent solar cells was performed using halide perovskite[45,47] compositions of $Cs_{0.15}FA_{0.85}Pb(I_{0.85}Br_{0.15})_3$ combined with printed pillars. XRD confirmed that the presence of pillars did not affect the perovskite crystallinity, showing sharp peaks at 14.15°, 20.13°, 32.03°, and 40.92° corresponding to the (100), (101), (201), and (022) crystallographic planes, with no PbI_2 residue detected (Fig. 4a and b).[10] The devices were completed with Spiro-OMeTAD and $MoO_x/Au/MoO_x$ electrodes (Fig. 4c), achieving $V_{oc} \approx 1.0$ V, $J_{sc} = 13–15$ mA cm^{-2}, and FF = 62–67%. Decreasing the pillar distance slightly reduced J_{sc} and caused a minor decrease in V_{oc} due to non-radiative recombination at the pillar–perovskite interfaces (Fig. 4d), as observed from the TRPL measurements.

EQE was measured for the semi-transparent cells, which follows the same trend as the absorption spectra, as shown in Fig. 4e–f. The variation in photovoltaic parameters with continuous illumination was also measured and is presented in the SI Fig. S16 and Table ST2. The reference opaque devices were fabricated with 70 nm gold contacts, and their PV parameters are shown in the supporting Table ST3 and Fig. S17.

The fabricated devices exhibited tunable high transmission (400–800 nm) (Fig. 5a). The calculated light utilization efficiency (LUE) increased with pillar distance, reaching 3.23 for 1000 pillars, surpassing the reported BIPV threshold of 2.5 (Fig. 5b).[2,12,48] The trade-off between the V_{oc} and LUE is observed in the measurement, but high values for both make these cells very appropriate for BIPV applications. The transparency of the complete cell with different pillar coverage was measured from the PET side and shown in Fig. S18. The charge extraction measurements show a similar rate of recombination for all pillar distances, while a slightly slower recombination rate for the pristine samples (Fig. 5c).

Interestingly, the bending capabilities were significantly improved due to the presence of the pillars: the pristine devices lost ~50% efficiency at a bending radius of 10 mm, whereas the pillar-based devices retained 85–90%. Furthermore, the efficiency remained 80–98% even after 1000 bending cycles (Fig. 5d and e). Long-term stability tests under ambient conditions and illumination for 1200 hours showed that pristine devices
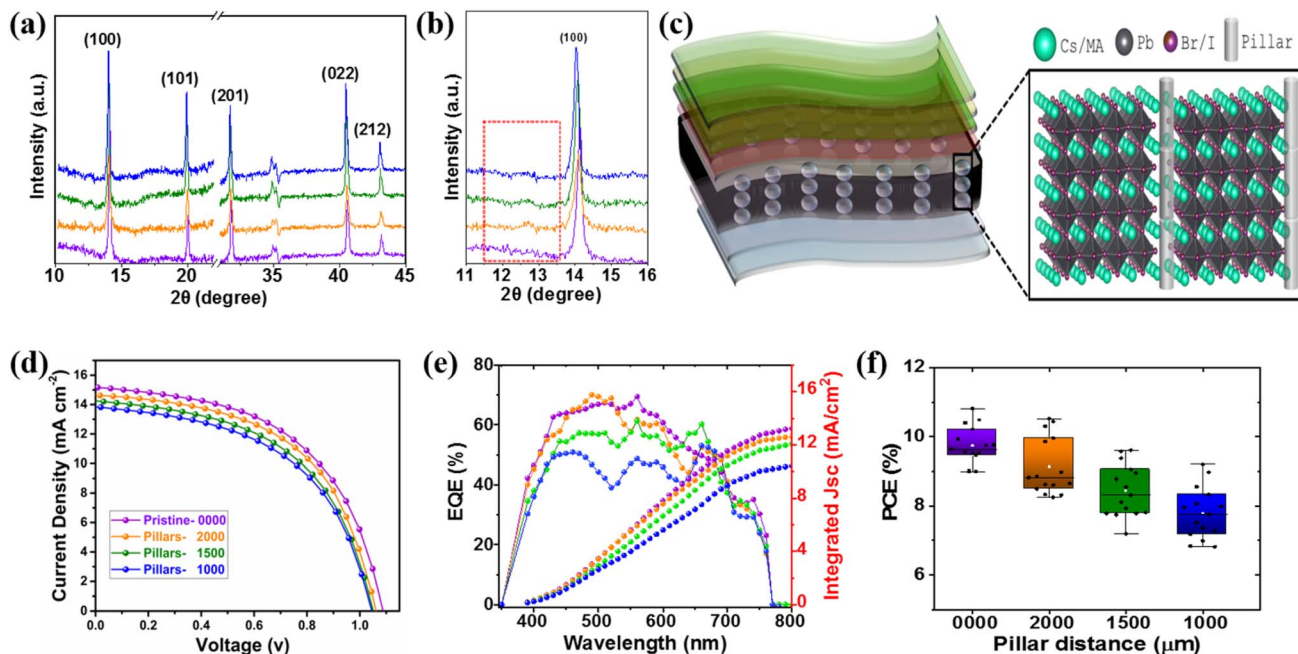
Fig. 4 (a) XRD spectrum of halide perovskite layers with and without pillars. (b) XRD spectrum of halide perovskite layers for the detection of PbI_2 peak. (c) Schematic structure of a semi-transparent device including 3D printed pillars. (d) J–V plot for cells with various densities of pillars. (e) The external quantum efficiency spectra and calculated integrated current distance curve for the various cells. (f) Variation in PCE for 16 cells with different densities of pillars.

degraded to ~40% of the initial PCE, compared to ~80% for pillar-embedded devices (Fig. 5f). The improved stability in pillar-based cells is attributed to the mitigation of defect formation and transportation, which enhances both the bulk and interface properties.

Overall, the integration of 3D-printed polymer pillars provides tunable transparency, mechanical durability, and long-term stability without compromising photovoltaic performance, making this approach highly promising for BIPV and flexible energy-harvesting applications.
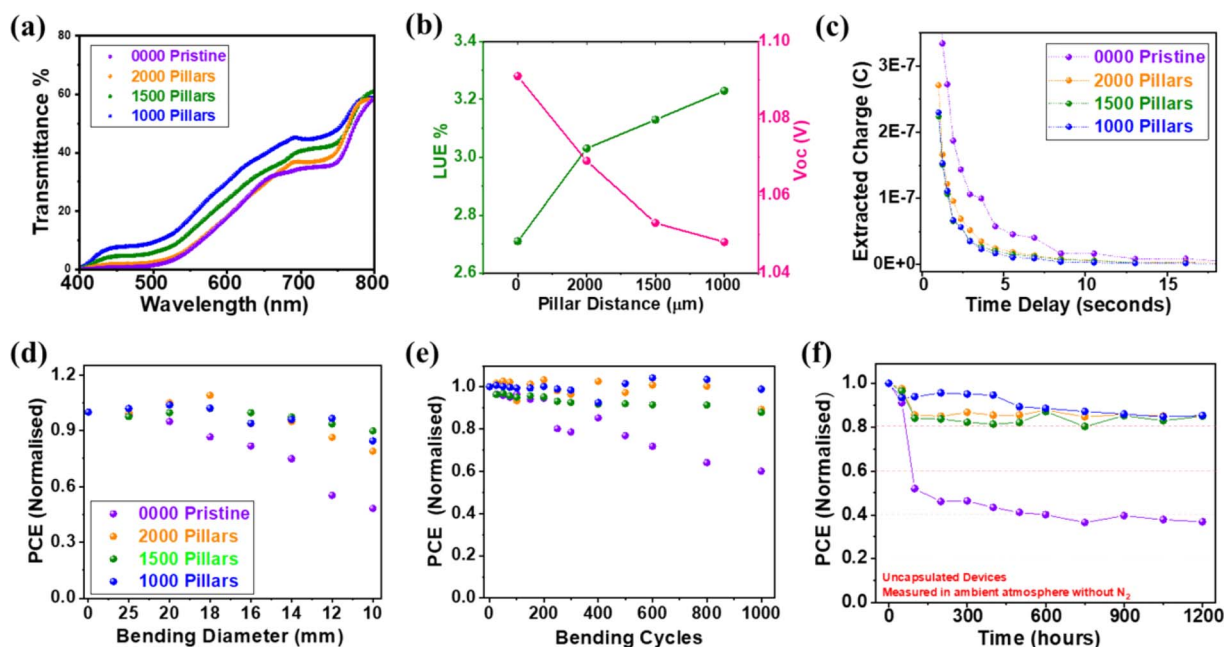

Fig. 5 (a) Transparency of the complete devices, including the transparent contact. (b) LUE and open circuit voltage as a function of pillar distance. (c) Charge extraction measurements. (d) PCE as a function of bending diameter, (e) stability of the cells with bending cycles up to 1000 bends. (f) Stability measurements under ambient conditions and illumination (not constant) for 1200 h.
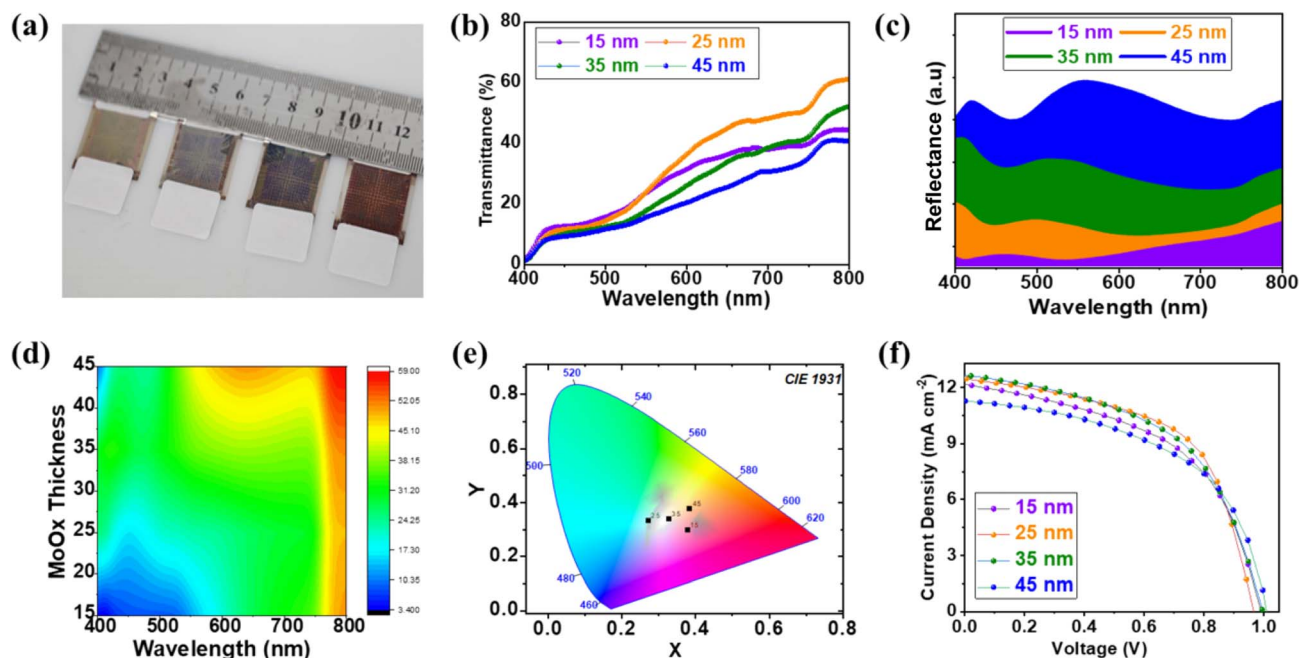
Fig. 6 (a) Colourful semi-transparent flexible devices, showing different colours. (b) Transparency spectra of different devices with different colours. (c) Reflection spectra of colourful semi-transparent flexible devices in the visible region. (d) 2D contour plots of reflectance as a function of the wavelength and the thickness of the top MoO_x, when illuminated from the DMD electrode side. (e) Colour coordinates generated from the measured (black squares) spectral reflectance curves, described on the CIE 1931 chromaticity diagram when illuminated from the top. (f) $J-V$ curve for the different coloured cells measured with AM 1.5 G source.

Tuning the colour of semi-transparent cells

After achieving semi-transparent cells, we aimed to create semi-transparent cells with tunable colours. This was achieved by varying the thickness of the transparent electrode, without altering the perovskite composition or introducing an additional layer. The top transparent electrode consists of an oxide/metal/oxide structure, with gold sandwiched between two layers of oxide.[49] The bottom layers of metal oxide also provide the adhesion to the below organic layers.[50] To tune the colour of the device, we changed the thickness of the top MoO_x layer.

Experiments with pristine samples (Fig. S19) led to the selection of 1000-pillar semi-transparent cells for the fabrication of the coloured device. By varying the MoO_x thickness from 15 to 45 nm, different colours were achieved while maintaining high transparency (>30%), which was controlled by the pillar distance and MoO_x thickness (Fig. 6a and b). Reflectance spectra (Fig. 6c and d) confirmed that colour tuning arises from constructive interference in an asymmetric Fabry–Perot cavity formed by the MoO_x-metal structure (Fig. S20). A detailed explanation of the reflection mechanism for colour tunability is presented in the supporting data. Chromaticity analysis (Fig. 6e) showed colour transitions from purple to yellow with increasing thickness, consistent with experimental and simulated data. Complete coloured cells were fabricated (Fig. S21 and S22), with power conversion efficiencies of ~6–8% for 15, 25, 35, and 45 nm MoO_x, respectively, as shown in Table ST4. The corresponding $J-V$ curves are shown in Fig. 6f. These results demonstrate controllable optical properties and photovoltaic performance through modulation of MoO_x thickness.

Conclusions

In this work, we demonstrated that visible light transparency can be enhanced without altering the perovskite bandgap or chemical structure by incorporating 3D-printed pillar architectures. A non-toxic, solvent-free, and fully UV-curable ink was developed for polymeric pillar printing, enabling scalable and environmentally friendly fabrication. In addition, a low-temperature process was developed and optimized to produce a tin-based ETL suitable for both rigid and flexible substrates. The resulting devices, with the architecture PEN/ITO/SnO_x/polymer pillars/perovskite/Spiro/MoO_x/Au/MoO_x, achieved high efficiencies (~10%) combined with excellent transparency (>30%) across the visible spectrum (400–800 nm). The flexible solar cells exhibited outstanding bending durability and long-term operational stability, making them promising for applications on curved and unconventional surfaces. Furthermore, by tuning the dielectric (oxide) thickness in the DMD structure, colour-tunable devices were realized, and the underlying optical mechanism was systematically studied. This proof of concept highlights the potential for printable, semi-transparent, and colour-controlled perovskite solar cells. Future improvements, particularly through the incorporation of barrier layers and encapsulation, are expected to further enhance device performance and stability.

Conflicts of interest

The authors declare that they have no conflict of interest.

Data availability

The data that support the findings of this study are available in the supplementary information (SI). Supplementary information: all relevant experimental data, as well as the detailed fabrication procedure and the reflectance model used. See DOI: https://doi.org/10.1039/d5el00153f.

Acknowledgements

References

1 A. S. R. Bati, Y. L. Zhong, P. L. Burn, M. K. Nazeeruddin, P. E. Shaw and M. Batmunkh, *Commun. Mater.*, 2023, **41**(4), 1–24.

2 T. M. Koh, H. Wang, Y. F. Ng, A. Bruno, S. Mhaisalkar and N. Mathews, *Adv. Mater.*, 2022, **34**, 2104661.

3 T. Wallach and L. Etgar, *Appl. Phys. Rev.*, 2025, **12**, 011314.

4 T. G. Allen, E. Ugur, E. Aydin, A. S. Subbiah and S. De Wolf, *ACS Energy Lett.*, 2024, **10**, 238–245.

5 D. Wang, Z. Liu, Y. Qiao, Z. Jiang, P. Zhu, J. Zeng, W. Peng, Q. Lian, G. Qu, Y. Xu, Y. Zhang, F. Li, L. Yan, X. Wang, Y. G. Wang, A. K. Y. Jen and B. Xu, *Joule*, 2025, **9**, 101815.

6 Y. Gao, K. Huang, C. Long, Y. Ding, J. Chang, D. Zhang, L. Etgar, M. Liu, J. Zhang and J. Yang, *ACS Energy Lett.*, 2022, **7**, 1412–1445.

7 M. J. Paik, Y. Y. Kim, J. Kim, J. Park and S. Il Seok, *Joule*, 2024, **8**, 2073–2086.

8 A. S. Subbiah, N. Mathews, S. Mhaisalkar and S. K. Sarkar, *ACS Energy Lett.*, 2018, **3**, 1482–1491.

9 A. P. Muthukrishnan, J. Lee, J. Kim, C. S. Kim and S. Jo, *RSC Adv.*, 2022, **12**, 4883–4890.

10 B. Sharma, R. Garai, M. A. Afroz, T. Sharma, S. Choudhary, R. K. Singh and S. Satapathi, *Adv. Energy Mater.*, 2024, **14**, 2402473.

11 M. J. Jeong, J. H. Lee, C. H. You, S. Y. Kim, S. Lee and J. H. Noh, *Adv. Energy Mater.*, 2022, **12**, 2200661.

12 D. B. Ritzer, B. Abdollahi Nejand, M. A. Ruiz-Preciado, S. Gharibzadeh, H. Hu, A. Diercks, T. Feeney, B. S. Richards, T. Abzieher and U. W. Paetzold, *Energy Environ. Sci.*, 2023, **16**, 2212–2225.

13 L. Xiao, G. Huang, H. Zhang, X. Zhang, Y. Li, S. Li, T. Jiang, B. Han, Y. Zhang and H. Zhou, *Sol. RRL*, 2022, **6**, 2100818.

14 C. tan, D. Liu, M. Bates, M. C. Barr and R. R. Lunt, *Joule*, 2019, **3**, 1803–1809.

15 I. Levine, O. G. Vera, M. Kulbak, D. R. Ceratti, C. Rehermann, J. A. Márquez, S. Levcenko, T. Unold, G. Hodes, I. Balberg, D. Cahen and T. Dittrich, *ACS Energy Lett.*, 2019, **4**, 1150–1157.

16 I. Levine, A. Al-Ashouri, A. Musiienko, H. Hempel, A. Magomedov, A. Drevilkauskaite, V. Getautis, D. Menzel, K. Hinrichs, T. Unold, S. Albrecht and T. Dittrich, *Joule*, 2021, **5**, 2915–2933.

17 S. Lie, A. Bruno, L. H. Wong and L. Etgar, *ACS Appl. Mater. Interfaces*, 2022, **14**, 11339–11349.

18 A. Kessel and J. J. Jasieniak, *J. Phys. Chem. Lett.*, 2024, **15**, 9894–9904.

19 S. Rahmany and L. Etgar, *ACS Energy Lett.*, 2020, **5**, 1519–1531.

20 N. K. Pendyala, S. Magdassi and L. Etgar, *Sol. RRL*, 2023, **7**, 2200988.

21 N. K. Pendyala, S. Magdassi and L. Etgar, *ACS Appl. Mater. Interfaces*, 2021, **13**, 30524–30532.

22 J. Jin, J. Zhang, J. Zhang, S. Zou, Y. Xin, B. Du, X. Yan and J. Huang, *Adv. Energy Mater.*, 2025, **15**, e01994.

23 R. Keshavarzi, F. Hajisharifi, Z. Saki, M. Omrani, R. Sheibani, N. Afzali, M. Abdi-Jalebi, L. Vesce and A. Di Carlo, *Nano Today*, 2025, **61**, 102600.

24 R. Pesch, A. Diercks, J. Petry, A. Welle, R. Pappenberger, F. Schackmar, H. Eggers, J. Sutter, U. Lemmer and U. W. Paetzold, *Sol. RRL*, 2024, **8**, 2400165.

25 T. Abzieher, D. T. Moore, M. Roß, S. Albrecht, J. Silvia, H. Tan, Q. Jeangros, C. Ballif, M. T. Hoerantner, B. S. Kim, H. J. Bolink, P. Pistor, J. C. Goldschmidt, Y. H. Chiang, S. D. Stranks, J. Borchert, M. D. McGehee, M. Morales-Masis, J. B. Patel, A. Bruno and U. W. Paetzold, *Energy Environ. Sci.*, 2024, **17**, 1645–1663.

26 J. Zheng, W. Zhu, J. Xiong, Q. Wang, R. Xuan, X. Sun, X. Gan, X. Liu, L. Huang, Y. Zhu and J. Zhang, *ACS Appl. Mater. Interfaces*, 2024, **17**, 1110–1118.

27 E. Almeida, M. Alexandre, I. M. Santos, R. Martins, H. Águas and M. J. Mendes, *ACS Omega*, 2024, **9**, 42839–42849.

28 Z. Li, S. Li, J. Yan, J. Peng and T. Ma, *Nat. Rev. Clean Technol.*, 2025, **13**(1), 216–226.

29 J. Bing, L. G. Caro, H. P. Talathi, N. L. Chang, D. R. Mckenzie and A. W. Y. Ho-Baillie, *Joule*, 2022, **6**, 1446–1474.

30 J. Heo, I. Jung, H. Park, J. H. Han, H. Kim, H. Park, J. S. Park, H. Jeon, K. T. Lee and H. J. Park, *Adv. Opt. Mater.*, 2022, **10**, 2101696.

31 H. Wang, H. A. Dewi, T. M. Koh, A. Bruno, S. Mhaisalkar and N. Mathews, *ACS Appl. Mater. Interfaces*, 2020, **12**, 484–493.

32 H. Wang, J. Li, H. A. Dewi, N. Mathews, S. Mhaisalkar and A. Bruno, *J. Phys. Chem. Lett.*, 2021, **12**, 1321–1329.

33 H. Eggers, S. Gharibzadeh, S. Koch, F. Schackmar, D. B. Ritzer, T. Abzieher, B. S. Richards, C. Erban and U. W. Paetzold, *Sol. RRL*, 2022, **6**, 2100897.

34 Q. Yang, W. Duan, A. Eberst, B. Klingebiel, Y. Wang, A. Kulkarni, A. Lambertz, K. Bittkau, Y. Zhang, S. Vitusevich, U. Rau, T. Kirchartz and K. Ding, *J. Mater. Chem. A*, 2024, **12**, 14816–14827.

35 A. Lorusso, S. Masi, C. Triolo, F. Mariano, S. Muia, A. Cannavale, Y. Duan, M. Anni, M. L. De Giorgi, S. Patané, O. Selmi, I. Mora-Seró, S. De Leo and M. Mazzeo, *ACS Energy Lett.*, 2024, **9**, 1923–1931.

36 V. Sharma, P. Kumar, A. Kumar, S. Surbhi, K. Asokan and K. Sachdev, *Sol. Energy Mater. Sol. Cells*, 2017, **169**, 122–131.

37 Q. Jiang, L. Zhang, H. Wang, X. Yang, J. Meng, H. Liu, Z. Yin, J. Wu, X. Zhang and J. You, *Nat. Energy*, 2016, **21**(2), 1–7.

38 M. R. Kokaba, Y. Ahmed, V. Yeddu, D. Zhang, P. Moazzezi, V. Kamraninejad, S. Dayneko, S. B. Reinecke, A. Amaro, B. Villarejo, A. Shyla, S. Malek and M. I. Saidaminov, *Sol. RRL*, 2024, **8**, 2301013.

39 A. Singha, A. Paul, S. Koul, V. Sharma, S. Mallick, K. R. Balasubramaniam and D. Kabra, *Sol. RRL*, 2023, **7**, 2300117.

40 M. Saliba, J. P. Correa-Baena, C. M. Wolff, M. Stolterfoht, N. Phung, S. Albrecht, D. Neher and A. Abate, *Chem. Mater.*, 2018, **30**, 4193–4201.

41 L. Z. Liu, X. L. Wu, F. Gao, J. C. Shen, T. H. Li and P. K. Chu, *Solid State Commun.*, 2011, **151**, 811–814.

42 C. Li, H. Sun, D. Dou, S. Gan and L. Li, *Adv. Energy Mater.*, 2024, **14**, 2401883.

43 Y. Yang, H. Huang, L. Yan, P. Cui, Z. Lan, C. Sun, S. Du, X. Wang, C. Yao, S. Qu, Q. Zhang, M. Wang, X. Zhao and M. Li, *Adv. Energy Mater.*, 2024, **14**, 2400416.

44 H. Afshari, S. Sourabh, S. A. Chacon, V. R. Whiteside, R. C. Penner, B. Rout, A. R. Kirmani, J. M. Luther, G. E. Eperon and I. R. Sellers, *ACS Energy Lett.*, 2023, **8**, 2408–2413.

45 W. Tan, A. R. Bowring, A. C. Meng, M. D. McGehee and P. C. McIntyre, *ACS Appl. Mater. Interfaces*, 2018, **10**, 5485–5491.

46 J. J. Jeronimo-Rendon, S. H. Turren-Cruz, J. Pascual, D. Di Girolamo, M. A. Flatken, H. Köbler, W. Hempel, M. Li, A. Di Carlo, P. P. Boix, I. Mora-Seró, A. Abate and M. Saliba, *Adv. Funct. Mater.*, 2024, **34**, 2313928.

47 B. G. H. M. Groeneveld, S. Adjokatse, O. Nazarenko, H. H. Fang, G. R. Blake, G. Portale, H. Duim, G. H. ten Brink, M. V. Kovalenko and M. A. Loi, *Energy Technol.*, 2020, **8**, 1901041.

48 E. Annabi Milani, M. Piralaee and A. Asgari, *Sci. Rep.*, 2023, **13**, 1–9.

49 A. Manekkathodi, B. Chen, J. Kim, S. W. Baek, B. Scheffel, Y. Hou, O. Ouellette, M. I. Saidaminov, O. Voznyy, V. E. Madhavan, A. Belaidi, S. Ashhab and E. Sargent, *J. Mater. Chem. A*, 2019, **7**, 26020–26028.

50 E. Magliano, P. Mariani, A. Agresti, S. Pescetelli, F. Matteocci, B. Taheri, A. Cricenti, M. Luce and A. Di Carlo, *ACS Appl. Energy Mater.*, 2023, **6**, 10340–10353.